PERGAMON

International Journal of Multiphase Flow 28 (2002) 1021–1046

International Journal of Multiphase Flow

www.elsevier.com/locate/ijmulflow

Gas–solid two-phase flow in a triple bifurcation lung airway model ☆

Z. Zhang [a], C. Kleinstreuer [b,*], C.S. Kim [c]

[a] *Center for Environmental Medicine and Lung Biology, University of North Carolina at Chapel Hill, Chapel Hill, NC 27599, USA*

[b] *Department of Mechanical and Aerospace Engineering, North Carolina Sate University, Campus Box 7910, 3211 Broughton Hall, Raleigh, NC 27695-7910, USA*

[c] *Human Studies Division, National Health and Environmental Effects Research Laboratory, US EPA, Research Triangle Park, NC 27711, USA*

Received 27 April 2001; received in revised form 15 December 2001

Abstract

Laminar oscillatory flow as well as micron-particle transport and wall deposition in a triple bifurcation airway model have been simulated using a validated finite-volume code with user-enhanced programs. Three realistic breathing patterns, i.e., resting, light activity and moderate exercise, were considered. Transient air flow, particle transport, and wall deposition results are shown and summarized in terms of regional particle deposition efficiencies (DEs). The effects of skewed inlet profiles on the flow field and particle deposition were recorded as well. Particle deposition may increase under cyclic flow conditions, i.e., DE-values are typically larger for cyclic flow than for steady flow evaluated at the *mean* flow rate of a given inhalation or exhalation pulse. While particles deposit mainly around the carinal ridges, i.e., flow dividers, during inspiratory flow due to direct impaction, they deposit on the tubular surfaces during exhalation because of strong secondary flows. Moreover, particle deposition during exhalation is much lower than for inhalation at the same local Stokes number. The comparisons of DEs among different lung generations or bifurcation areas for both cyclic inhalation and exhalation show that DEs in the third bifurcation region may be quite different from those at previous bifurcations due to upstream geometry and flow effects.

Keywords: Large bronchial airways; Aerosol transport and deposition; Computational two-phase flow

☆ Presented in part at the International Conference on Multiphase Flow (ICMF-2001), New Orleans, May 23–June 1, 2001.

* Corresponding author. Tel.: +1-919-515-5216; fax: +1-919-515-7968.

E-mail address: ck@eos.ncsu.edu (C. Kleinstreuer).

URL: http://www.mae.ncsu.edu/research/ck_CFPDlab/index.html.

0301-9322/02/$ - see front matter
PII: S0301-9322(02)00011-3

1. Introduction

Accurate information on local and regional aerosol depositions in the upper bronchial tree under realistic breathing conditions is most valuable for researchers of dosimetry-and-health-effect studies. They include deposition efficiencies (DEs) of toxic particles to assess health risk factors as well as desired surface concentrations of drug aerosols to evaluate therapeutic effects. Employing the widely used symmetric Weibel configuration of generations G3–G6 (G0 is the trachea, Weibel, 1963), three realistic breathing patterns, i.e., resting, light activity plus approximate sine-waveform, and moderate exercise have been considered (Fig. 1(a)–(c)). Associated with the inlet flow waveforms are monodispersed, uncharged, spherical micron-particles with a dilute suspension loading which reflects the filtering effect of the upper respiratory tract.

Earlier theoretical and experimental works were summarized and discussed by Zhang et al. (1997), who simulated the impact of different bifurcation angles and parabolic vs. uniform inlet velocity profiles on particle DEs as a function of the inlet Stokes number. Presently, the state-of-the-art is represented by theoretical steady three-dimensional (3D) air flow and particle deposition results for double bifurcations with different geometric features (cf. Comer et al., 2000, 2001a,b; Zhang et al., 2000) as well as particle deposition measurements of Kim and Garcia (1991a,b), and Kim and Fisher (1999). The cyclic inhalation/exhalation experiments with a single bifurcation clearly showed that transient flow in, say, a triple bifurcation has to be considered in order to model part of the upper bronchial tree more realistically.

In this study, the focus is on the effects of three different breathing rates on local and regional particle depositions in a representative triple lung airway bifurcation. Specifically, deposition patterns and efficiencies are compared for cyclic inhalation and cyclic exhalation.

2. Theory

2.1. Bifurcation geometry and field equations

The block structure, finite volume mesh and the subdivision of the systems of a representative triple bifurcation are given in Fig. 1(b)–(d), where the geometric data are provided in Table 1. The tubular model is rigid and symmetric with respect to the $z = 0$ plane and the y-axis.

The realistic tube model represents the third to sixth generation human respiratory airways according to Weibel's lung classification scheme (Weibel, 1963). The reasons that we chose these generations (i.e., G3–G6) for simulation are: (i) to compare particle deposition data with the experimental data for G3–G5 (Kim and Fisher, 1999); (ii) to avoid the turbulent jet effect of the larynx (Katz and Martonen, 1999); and (iii) to reduce the effect of cartilaginous rings which appear in the larynx, trachea (G0), and main bronchi (G1) (Oho and Amemiya, 1980). The rings may become less protruded and are insignificant starting from G3.

The parameters of the inlet flow waveforms (Fenn and Rahn, 1965) and associated particle characteristics are summarized in Table 2. The transient 3D fluid-particle transport equations are (Kleinstreuer, 1997):

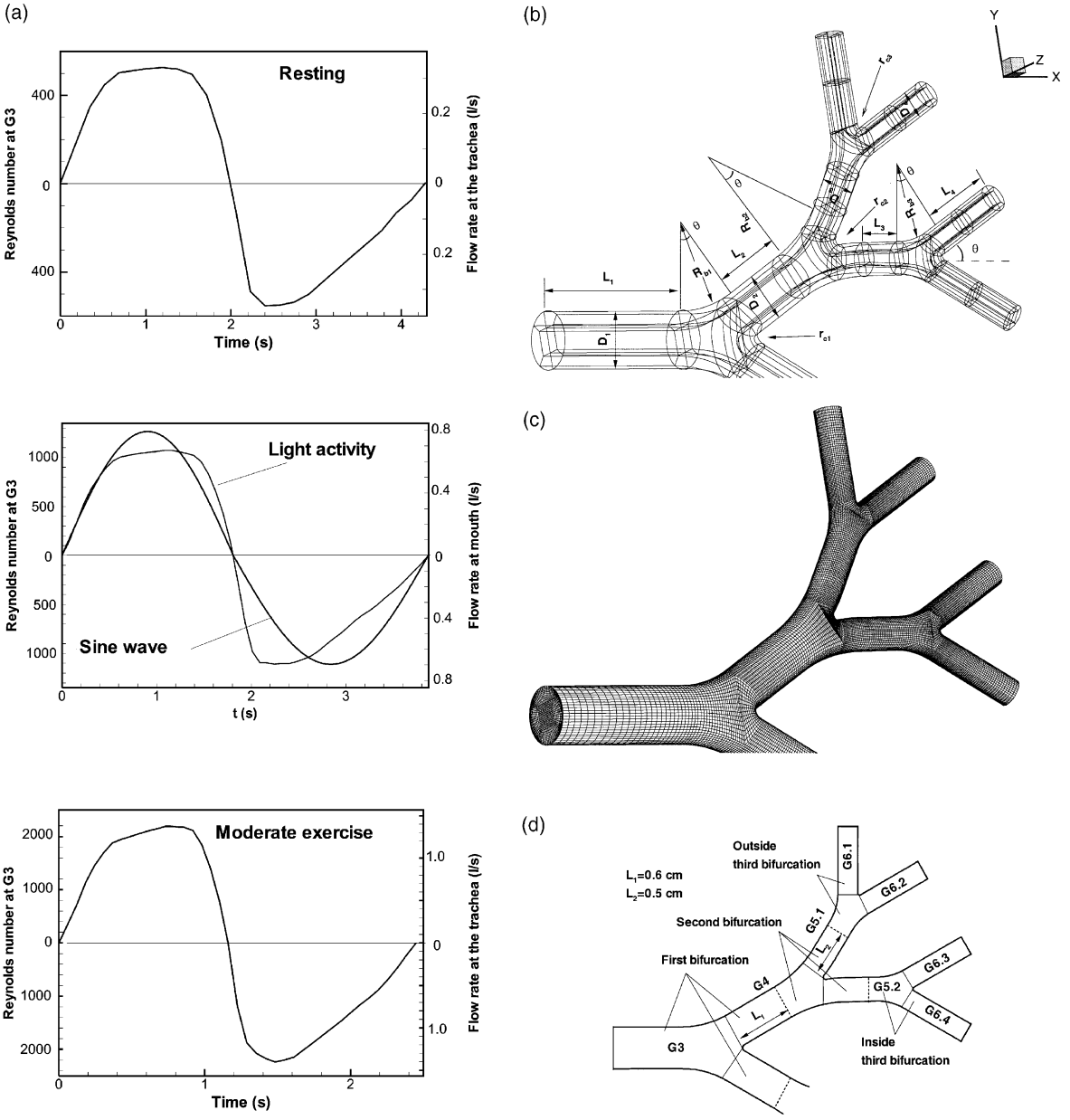

Fig. 1. Schematics of flow input waveform and symmetric triple bifurcation geometry: (a) flow input waveform; (b) block structure; (c) finite volume mesh; and (d) airway model segmentation (bifurcations and generations, the dashed line indicates the boundary of bifurcation).

Continuum

$$\nabla \cdot \vec{v} = 0 \tag{1}$$

Table 1
Geometric parameters for triple bifurcation model (Dimensions in centimeter)

	Bifurcation					
	First		Second		Third	
Parent duct diameter	D_1	0.6	D_2	0.5	D_3	0.35
Daughter duct diameter	D_2	0.5	D_3	0.35	D_4	0.29
Length of ducts	L_1	2.4	L_3	0.437	L_4	0.928
	L_2	0.836	L_3	0.437	L_4	0.928
Bifurcation radius of curvature	R_{b1}	$2.7D_2$	R_{b2}	$4.7D_3$	R_{b3}	$2.7D_4$
Carinal radius of curvature	r_{c1}	$0.1D_2$	R_{c2}	$0.1D_3$	r_{c3}	$0.1D_4$
Bifurcation half angle	θ			30°		

Table 2
Representative respiration data and particle parameters

Physical state	Resting	Light activity	Moderate exercise	Light activity (sine-waveform)
Respiration rate for inhalation (Q_{in}, l/min)	15	30	60	30
Tidal volume (ml)	500	907	1153	907
Time ratio of inspiratory phase (t_{in}/t_{total})	0.47	0.46	0.474	0.46
Breathing frequency (cycle/min)	14	15.5	24.5	15.5
Womersley number at G3[a]	0.89	0.93	1.18	0.93
Strouhal number at G3[b]	0.002	0.0011	0.0009	0.0011
Mean Reynolds number at G3[c]				
Inspiration	388	805	1586	805
Expiration	340	696	1418	696
Peak Reynolds number at G3				
Inspiration	514	1070	2194	1264
Expiration	540	1108	2237	1093
Particle diameter (d_p, μm)	3–7	3–7	3–7	3–7
Particle density (ρ_p, kg/m^3)	500–5000	500–5000	500–2500	500–5000
Mean Stokes number at G3[d]				
Inspiration	0.002–0.13	0.005–0.27	0.01–0.26	0.005–0.27
Expiration	0.002–0.12	0.004–0.23	0.01–0.23	0.004–0.23

[a] Womersley number $Wo = r_0(\omega/\upsilon)^{1/2}$, where r_0 is the tube radius, ω is the angular frequency, and υ is the air kinematic viscosity.

[b] Strouhal number $Str = Wo^2/Re$

[c] Reynolds number $Re = UD/\upsilon$, where U is the mean velocity and D is the tube diameter.

[d] Stokes number $St = \rho_p d_p^2 U/(18\mu D)$.

Momentum

$$\frac{\partial \vec{v}}{\partial t} + (\vec{v}\cdot\nabla)\vec{v} = -\frac{1}{\rho}\nabla p + \nabla\cdot\left[\upsilon\left(\nabla\vec{v} + (\nabla\vec{v})^{\mathrm{tr}}\right)\right] \tag{2}$$

where $\vec{v}$ is the fluid velocity vector; ρ is the fluid density; p is the pressure and υ is the fluid kinematic viscosity. For the dilute particle suspension, a decoupled Eulerian–Lagrangian approach has been selected.

Particle trajectory equation

$$m_{\mathrm{p}} \frac{\mathrm{d}^2 \vec{x}_{\mathrm{p}}}{\mathrm{d}t^2} = \frac{1}{8} \pi d_{\mathrm{p}}^2 \rho C_{\mathrm{DP}} (\vec{v} - \vec{v}_{\mathrm{p}}) |\vec{v} - \vec{v}_{\mathrm{p}}| \tag{3a}$$

where m_{p} is the mass of a single particle, x_{p} is the displacement of the particle, d_{p} and $\vec{v}_{\mathrm{p}}$ are the particle diameter and velocity, respectively; C_{DP} is the drag coefficient given as (Clift et al., 1978)

$$C_{\mathrm{DP}} = C_{\mathrm{D}} / C_{\mathrm{slip}} \tag{3b}$$

where

$$C_{\mathrm{D}} = \begin{cases} 24/Re_{\mathrm{p}} & \text{for } 0.0 < Re_{\mathrm{p}} < 1.0 \\ 24/Re_{\mathrm{p}}^{0.646} & \text{for } 1.0 < Re_{\mathrm{p}} \leqslant 400 \end{cases} \tag{3c}$$

The local particle Reynolds number is $Re_{\mathrm{p}} = \rho |\vec{v} - \vec{v}_{\mathrm{p}}| d_{\mathrm{p}} / \mu$, where μ is the dynamic viscosity of the fluid. A correlation for the Cunningham correction (i.e. slip) factor, C_{slip}, in Eq. (3b) can be found in Clift et al. (1978).

The underlying assumptions for Eqs. (1) and (2) and their boundary conditions include laminar incompressible flow in a smooth rigid conduit. In most cases, fully developed velocity profiles in accordance with the given inhalation–exhalation pulse and associated particle distributions were prescribed as inlet conditions. Specifically, the inlet velocity profiles at G3 were determined by the analytic expression of transient developed flow in a straight tube, following the given input pulse expressed as Fourier series (Buchanan, 2000). Particles were released from the inlet tube G3 (cf. Fig. 1) and exit tubes G6.1–G6.4 during inspiration and expiration, respectively, at different time steps according to the given volumetric flow rate $Q(t)$ (see Fig. 1(a)). The probability density function for the inlet particle coordinate or the inlet particle concentration is proportional to the inlet axial velocity profile at that moment for each release time step. Such a type of inlet particle distribution was verified to be suitable for experimental analyses and data comparisons (Zhang and Kleinstreuer, 2001). The final number of released particles and the time interval for releasing were determined by increasing the inlet particle concentration and decreasing the time interval until the DE became independent of the number of particles and the time interval simulated. DE is defined as the ratio of the number of particles deposited in a given region to the total number *entering the region*. In total, approximately 18,000 and 25,000 particles were released during one inspiratory cycle and expiratory cycle, respectively. In addition, skewed inlet velocity profiles and the associated particle distributions, obtained from the simulation results of generations G1–G3, were also employed to investigate the effects of inlet conditions during cyclic inhalation. A uniform pressure condition was assigned at the outlets of the distal tubes G6. The small effects of non-uniform outlet pressures, which may occur in actual lung airways, were discussed in a previous study (Zhang et al., 2000).

Eq. (3a) describes non-interacting, spherical micron-particles where the drag is the dominant force, while the lift forces, the Faxen pressure term, the Basset history term, etc. are negligible because of non-rotating particles, a relatively low shear environment, high particle-to-fluid density ratios, and very small particle Reynolds numbers, i.e., $Re_{\mathrm{p}} < 1$. Particles touching the wall deposit

immediately because of the permanently moist wall surfaces. The effects of gravity were not considered because gravitational settling is only important for large particle sizes and low flow rates which occur at the lower airways (say, from generation G9 on) (Kim et al., 1983; Hofmann et al., 1995).

2.2. Numerical method

The numerical solution of the air flow equations (Eqs. (1) and (2)) was carried out employing a user-enhanced commercial finite-volume based program CFX4.3 (AEA Technology, 1998). The CFX4 is based on a structured, multiblock, body-fitted coordinate, discretization scheme. In the present simulation, the SIMPLEC algorithm with under-relaxation was employed to solve the flow equations. A higher-order upwind differencing scheme, which is second-order accurate in space, was selected to model the advective terms of the transport equations. A fully implicit backward difference was used for temporal discretization. The sets of linearized and discretized equations for all variables were solved using an algebraic multi-grid method. Three cycles were simulated before releasing particles in order to avoid start-up effects on the air-particle flow fields.

In a post-processing step, the particle transport equation (Eq. (3a)) was solved with user-specified drag relations and detailed particle tracking. Gear's backward differentiation formula was used to integrate particle trajectories for each time step with a converged transient flow field. After each iteration for each particle, the information about position, time, and three components of the velocity as well as the speed with which the particles cross the control volume boundaries was obtained.

The mesh was generated based on the surface information obtained from the CAD models of the experimental glass tube bifurcation models (Kim and Fisher, 1999). Utilizing the assumed symmetry condition about the bifurcation plane, the flow field simulation involved only the upper half of the bifurcation model (i.e., $z \geqslant 0$). The effect of flow symmetry on particle motion was also tested, i.e., no particles crossed the symmetric plane during the test run. The mesh topology was determined by refining the mesh until grid independence of the flow field solution was achieved. The final mesh of the triple configuration contained about 360,000 finite volumes. The computations were performed on an SGI Origin 2400 workstation with 24GB of RAM and 48×400 MHz CPUs. A fixed time step ($\Delta t = 0.02$ s) was selected to calculate flow fields and particle trajectories. The solution of the flow field at each time step was assumed converged when the dimensionless mass residual was negligible, i.e., (total mass residual)/(mass flow rate) $< 10^{-3}$. A typical run time for fluid flow and particle transport simulations for one cycle on a single processor was approximately 72 h.

2.3. Model validation

The present computational fluid-particle dynamics (CFPD) model has been validated with various experimental data sets for single as well as double bifurcations under steady flow conditions (Comer et al., 2000, 2001a,b). Here, the CFPD model is further validated for cyclic flow cases. DE of aerosols in double bifurcating glass models was determined experimentally assuming steady inhalation (Kim and Fisher, 1999) as well as cyclic flow conditions at frequencies between 15 and 50 cycles/min. The experimental method for cyclic inhalation or exhalation in

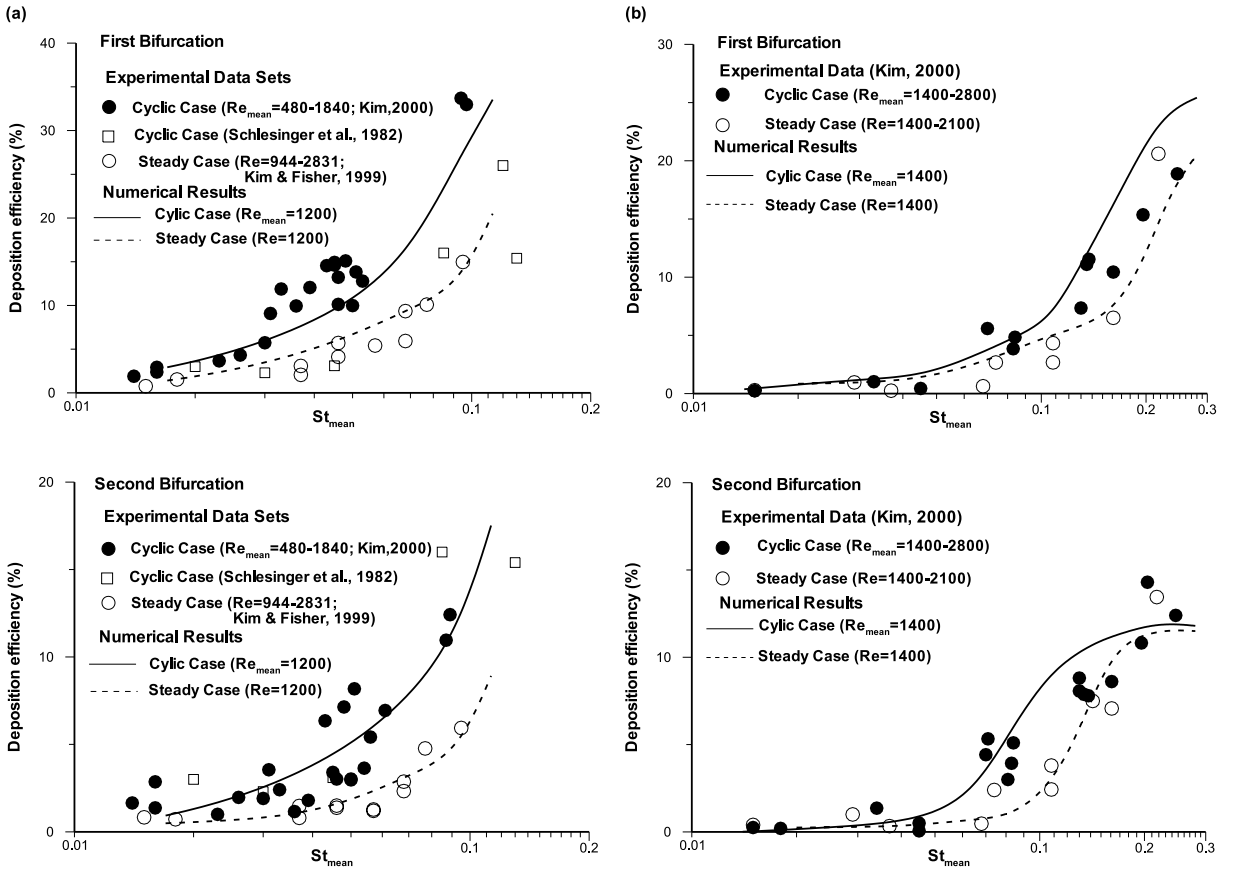

Fig. 2. Comparison of the predicted and experimental particle DEs in double bifurcation models under cyclic flow and constant flow: (a) aerosol inhalation phase; experimental data (Generations 3 and 4 only) of Schlesinger et al. (1982) are also shown for comparison; and (b) aerosol exhalation phase.

double bifurcation models was the same as the one described for single bifurcation models (Kim and Garcia, 1991a, 1991b). Fig. 2(a) and (b) shows the measured and CFPD-predicted DEs at two bifurcations for both cyclic and steady inspiratory and expiratory flows, respectively. Due to the difficulty in strictly controlling the flow rate and aerosol diameter, the Reynolds numbers varied measurably during the experiments. Furthermore, some differences between computational predictions and experimental measurements may be caused by subtle discrepancies in physical model geometries and deposition measurements. Thus, when neglecting the experimental Reynolds number effect and focusing on $DE = DE(St)$, the simulation results agree well with the experimental data. Both experimental and CFPD results show that the DEs for cyclic flow are higher than those for steady flow at the *mean* flow rate. This is because particle deposition increases rapidly near the peak flow, i.e., deposition is clearly a non-linear phenomenon while transient particle deposition during one point in the oscillatory cycle is quite similar to that in the *equivalent* steady flow due to the small Womersley and Strouhal numbers under normal breathing conditions. Moreover, the DEs during exhalation are much lower than those during inhalation for the

same Stokes number. The particle deposition data obtained by Schlesinger et al. (1982) in lung cast models under cyclic inhalation are also shown in Fig. 2(a) for comparison. In summary, the good agreements between experiments and predictions instill confidence that the present computer simulation model is sufficiently accurate to analyze oscillatory fluid-particle dynamics and particle deposition in a four-generation (i.e., triple bifurcation) lung airway model.

3. Results and discussion

3.1. Representative flow fields and particle distributions

Typical instantaneous air velocity vector fields (midplane and cross-sections) as well as particle distributions (cross-sections only) under resting and moderate exercise conditions are displayed in Figs. 3 and 4 for inhalation and exhalation, respectively. The particle motion in each section was captured just when these particles passed through the particular cross-section during a short time interval. The particle motion here is plotted for the mean Stokes number $St_{\text{mean}} = 0.12$ (St_{mean} is calculated based on the mean flow rate and the tube diameter at G3). The distances between these cross-sections and their corresponding upstream flow dividers are about 1.5 tube diameters.

Fig. 3(a) depicts the mid-plane velocity vector profiles and secondary flows in selected cross-sections as well as the corresponding particle motion at the time level with mean flow rate during decelerating *inspiratory* flow. The air stream splits at the first flow divider and a new boundary layer is generated at the inner wall of the first daughter tube, where the maximum axial velocity stays near the inner wall (see midplane view in Fig. 3(a)). Subsequently, the inside second daughter tube (i.e., G5.2 in Fig. 1(d)) experiences a higher air flow rate. Because the deflection of both the high and low flow portions from the first daughter tube G4 to the second daughter tubes G5.1 and G5.2 are relatively small and the local geometry is rather smooth, the velocity profiles in G5 are hardly skewed. In contrast, similar to the first bifurcation, the third daughter tubes encounter again asymmetric axial velocity profiles. Due to the small Womersley and Strouhal numbers in G3, the effect of unsteadiness is not pronounced and the inlet velocity profile is almost parabolic as it would be in the equivalent steady-state case.

After the first flow divider, the air streams are deflected and secondary motions are set up (cross-sectional views in Fig. 3(a)) due to the centrifugally induced pressure gradient. The secondary velocity field in cross-section A–A′ exhibits one distinct vortex which moves the high speed fluid up around the top of the tube toward the outside of the bifurcation and low speed fluid from the outside of the bifurcation along the symmetry plane toward the inside of the bifurcation. The secondary motions in B–B′ and C–C′ are somewhat different when compared to those in section A–A′ because of the geometric effects as well as the interaction between axial and secondary flows. Besides the vortex near the tube center, an additional co-rotating vortex moves around the top to the outside wall (see section B–B′ or C–C′). As expected, the strength of secondary flow in section C–C′ located in G5.2 where the flow rate is higher, is much stronger than in section B–B′ located in G5.1.

Cross-sectional particle distributions are useful to illustrate the impact of air flow structures, especially the effect of secondary flow, on particle motion. At cross-section A–A′ (Fig. 3(a)), the axial and secondary flow fields are good indicators for the local particle concentrations and

vortical motions, respectively. The skewed axial velocity profile causes high particle concentrations near the inner wall and top surface but lower concentrations near the outer wall and tube center. The particle flow field indicates one distinct vortical region which is similar to the secondary vortex. Under moderate exercise conditions, both axial and secondary air flows are more pronounced. Stronger centrifugal forces push, for the most part, particles from the core towards

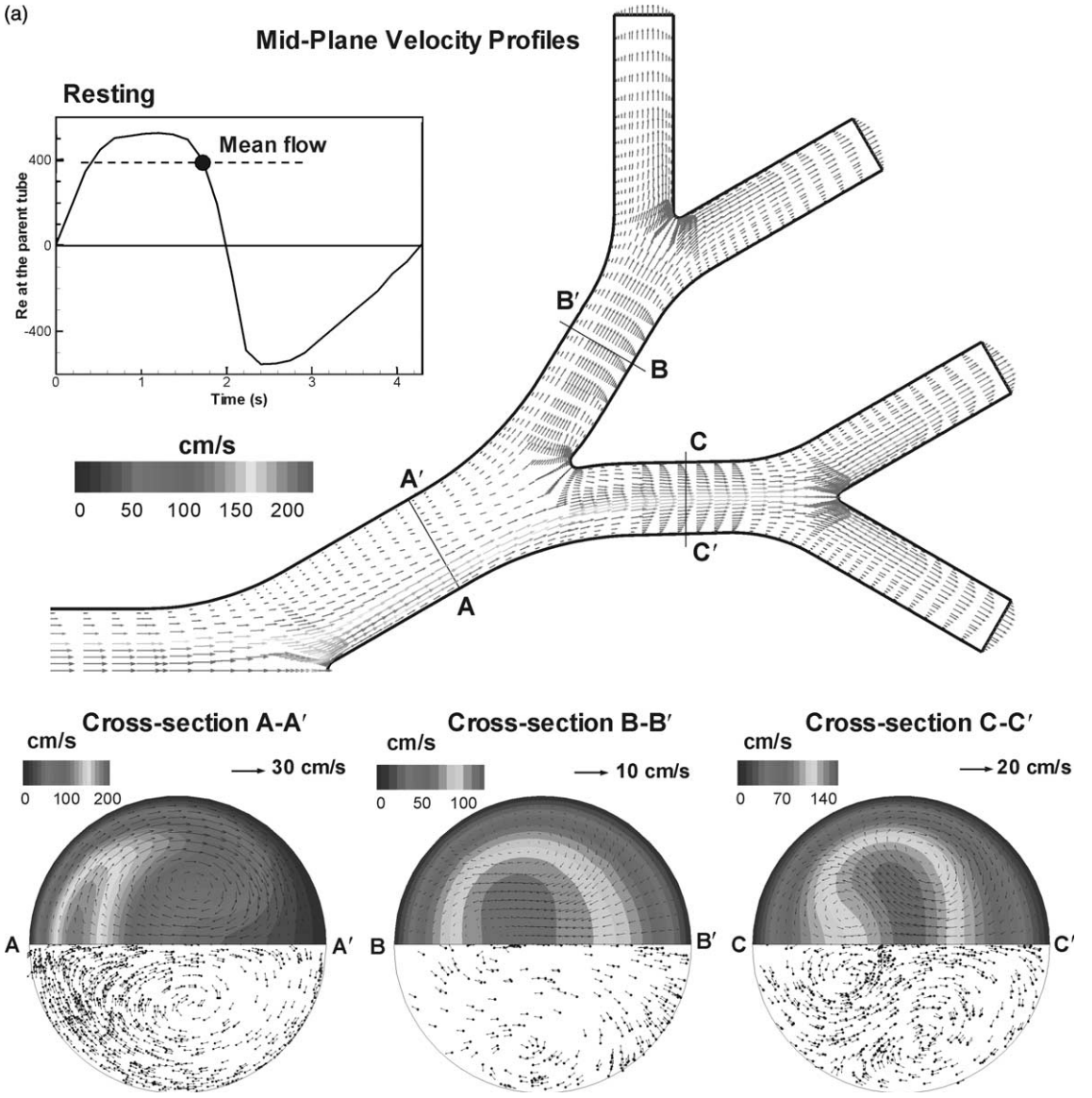

Fig. 3. Mid-plane velocity vectors, and axial velocity contours, secondary velocity vectors as well as particle distributions and flow directions at selected cross-sections at the time level of mean flow rate during the decelerating inspiratory phase for: (a) resting condition; and (b) moderate exercise condition.

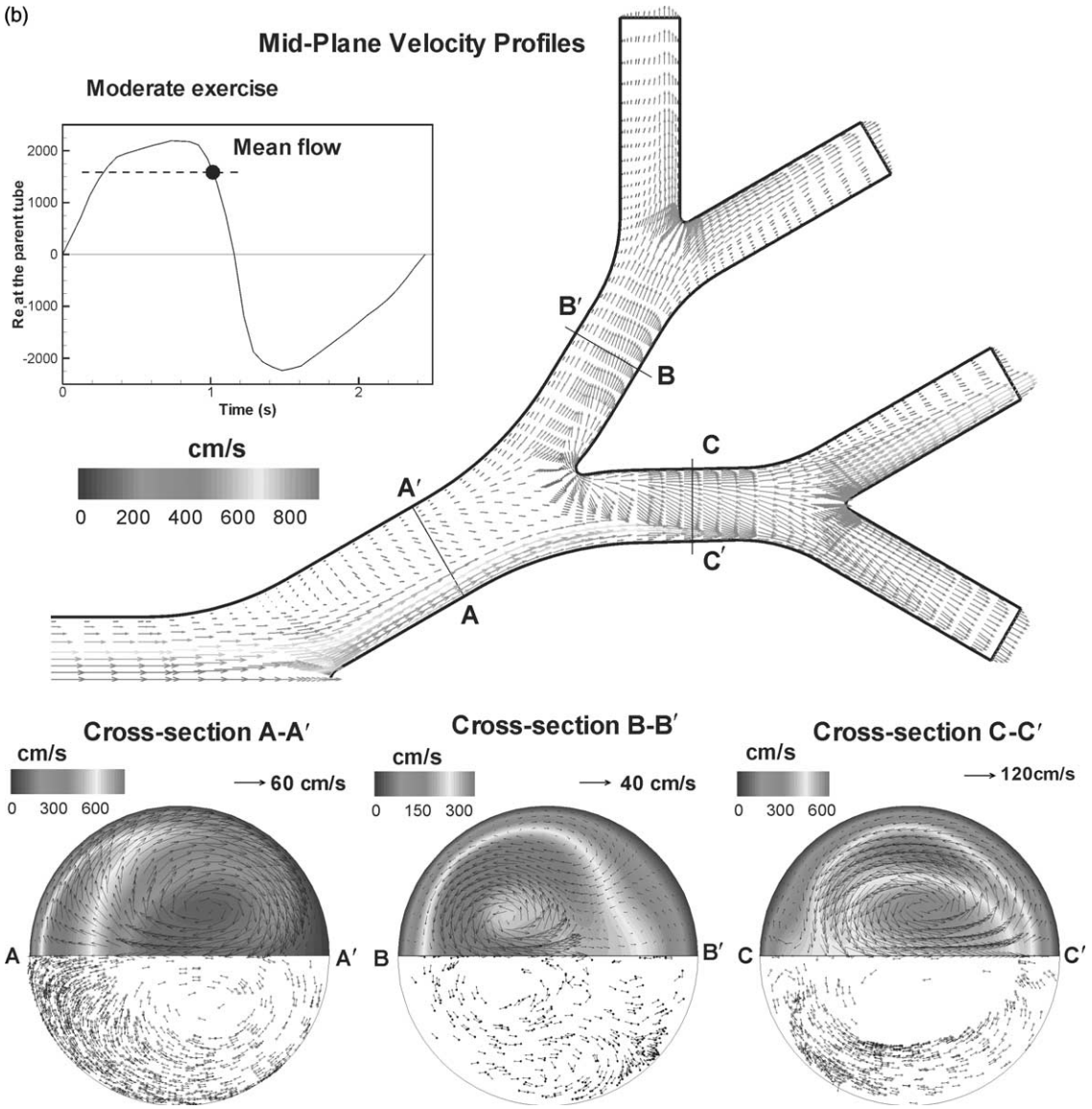

Fig. 3 (*continued*)

the airway walls (Fig. 3(b)). Specifically, the velocity profiles in the first daughter tube become more skewed due to boundary layer effects and convective acceleration, resulting in an increasing flow asymmetry between the two subsequent daughter branches. The distinct shear layer along the inside wall after the first divider (or carinal ridge) become thinner, and a recirculation zone is generated at the outer wall across from the carinal ridge area, which indicates the occurrence of a stagnation point for particle motion. Such a flow separation phenomenon is related to the geometric features of the geometric transition regions and the local Reynolds number. The flow separation is not observed at the second and third bifurcation because of the nearly constant

cross-sectional area at the second bifurcation and the low local Reynolds number at the third bifurcation. The secondary flow effect in the daughter tubes also increases with the respiration rate. The air of highest axial velocity in the inside second daughter tube rotates around the top and inside of the tube, lifting off from the symmetry plane for high ventilation intensities. Particles

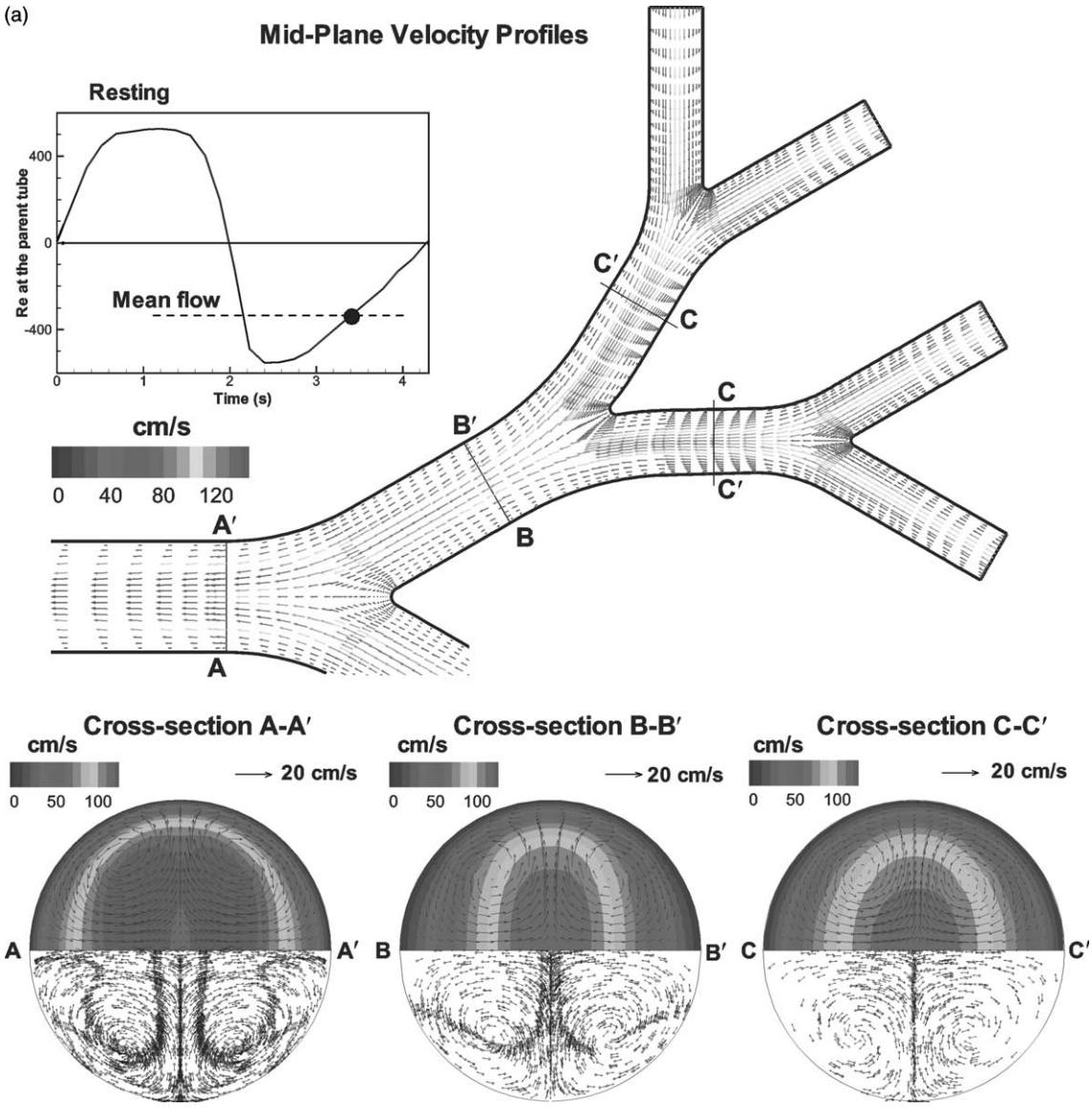

Fig. 4. Mid-plane velocity vectors, and axial velocity contours, secondary velocity vectors as well as particle distributions and flow directions at selected cross-sections at the time level of mean flow rate during the accelerating expiratory phase for: (a) resting condition; and (b) moderate exercise condition.

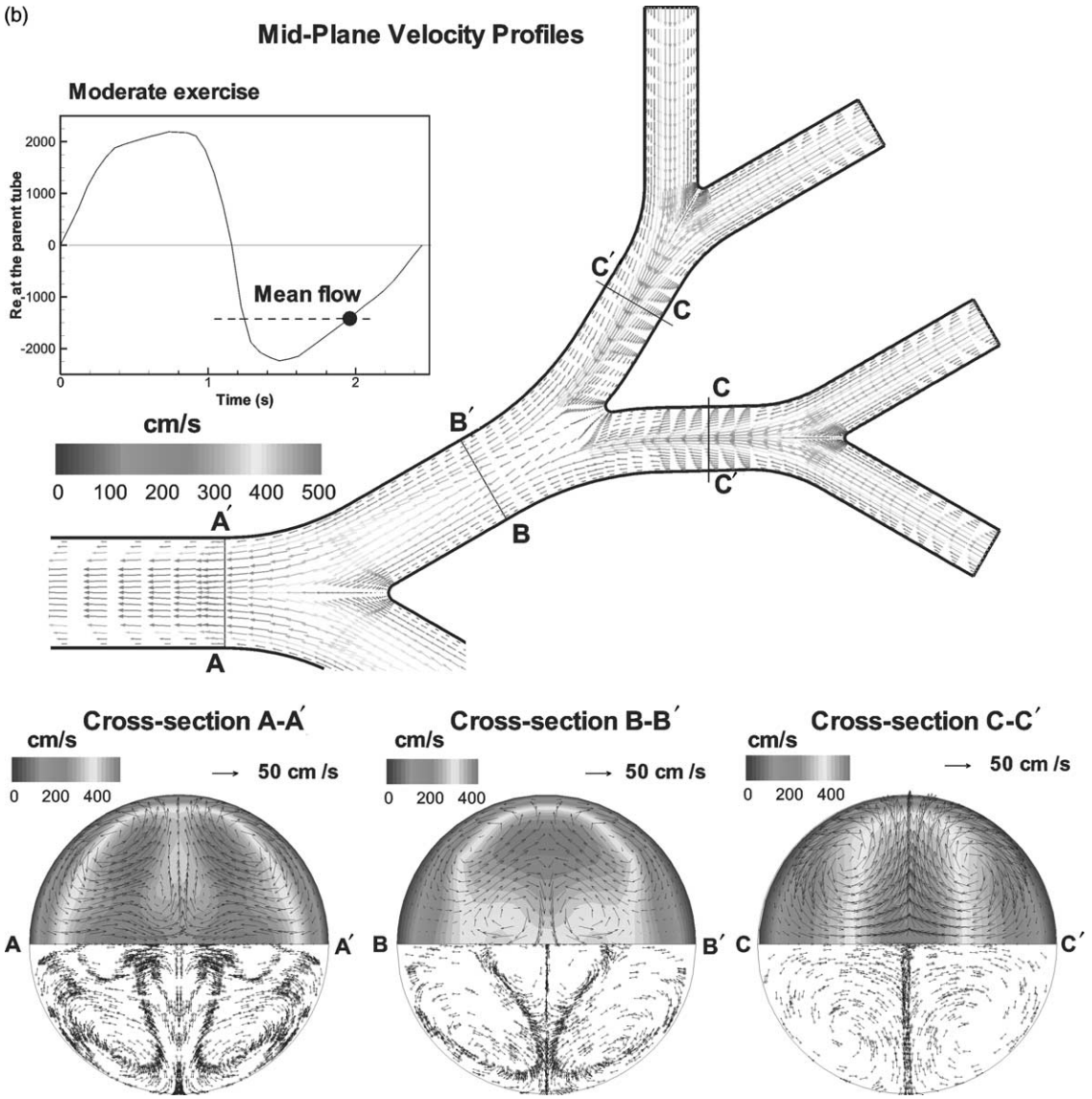

Fig. 4 (*continued*)

may not follow the secondary flow well due to the increased secondary vortex strength, and they may be pulled away from the vortex center owing to the centrifugal force. The vortex cores would be the regions of low particle concentration or even distinct particle-free zones.

Air flow during the *expiratory* phase through the bifurcation is quite different from inspiratory flow. Now, two streams from the daughter tubes merge so that just upstream of each flow divider velocity profiles in the bifurcation plane have indentations around the centers. Specifically, as shown in Fig. 4(a), the axial velocity profiles in the four third daughter tubes (G6.1–G6.4), which

function as inlets during exhalation, are almost parabolic because of the small Womersley number and the assumption of fully developed expiratory velocity profile at tube G3. The air streams through G6.1 and G6.2 as well as G6.3 and G6.4 join in tubes G5.1 and G5.2, respectively, with the maximum axial velocity being near the larger tube center. The situation is similar in upstream tubes G4 and G3. As a result of the Weibel geometry and the equal "inlet" conditions selected, the flow fields stay very symmetric in all branches. Velocity profiles with double peaks appear after the flow dividers, but they soon transform into marked centerline velocity peaks because of merging boundary layer effects. Like for inspiratory flow, the air stream is curved and therefore secondary motions develop when it turns a bend from the daughter tube to the downstream tube. Four symmetric secondary vortices are generated in each cross-section as shown in Fig. 4(a). The particles can essentially follow the secondary motion as shown especially in cross-section C–C′. Two large counter-rotating vortices convect particles from the wall region to the centerline where some particles are driven directly to the top/bottom surfaces. Therefore, secondary flow is the primary factor influencing the deposition of exhaled particles instead of axial flow. Expiratory particle motion is more sensitive to the variation of the instantaneous Stokes number during the cycle due to the more complicated secondary velocities. As indicated in cross-sections A–A′ and B-B′, some particles cannot follow the secondary flow due to the high vortex strength compared to that at section C–C′. The particles spiral away from the center of the vortex and some distinct bands of high particle concentrations are generated.

For expiratory flow under moderate exercise condition (Fig. 4(b)), a distinct velocity spike at the centerline is generated in tube G5.1 and tube G5.2; also, the merging length for the fast moving fluid increases in tube G4 compared with the situation in Fig. 4(a). It is the result of the interplay of convective acceleration and near-wall viscous forces, i.e., the boundary layer effect on the central axial velocity decreases with increasing Reynolds numbers. A low-velocity region is formed at the tube center in cross-section B–B′ due to the merging flow fields and the secondary flow effects. One of the more obvious changes is that the secondary flow and the associated particle motion become more complex. In addition to the four large vortices, four small secondary vortices are generated near the tube center as indicated in section A–A′ and more pronounced in section B–B′. The reason may be that the vortical flow cannot be developed as well as in the low mean flow rate case due to the stronger inertia effects. As a result, the particle motion is also more complex. Most particles spiral away from the center of the vortex and accumulate in convergence zones which are characterized by high strain rates and low vorticities. In fact, the distinct bands of high particle concentrations are generated between the vortex cores and convergence zones at which the variation of secondary flow is severe. These concentrated particle clouds may directly convect downstream. Clearly, particle distributions during exhalation are much more complex than during inhalation.

3.2. Particle deposition during inhalation

Particle deposition is an accumulative process during a given pulse. In order to investigate particle deposition under cyclic inhalation and exhalation independently, the inspiratory flow and expiratory flow for one breathing cycle shown in Fig. 1(a) are separated. An intermittent zero-flow period is assumed between two inspiratory or expiratory cycles to replace the equivalent expiratory or inspiratory time because moving particles in the present segmental bifurcation model

actually migrate into the other lung segments instead of moving back via exhalation or inhalation at the end of inspiration or expiration. There is still about 5% of the total inlet particles moving around in the tubes at the end of inspiration or expiration. After all (moving) particles have left the designated exit tubes after one additional inspiratory or expiratory pulse, the final particle deposition patterns for one inhalation or exhalation cycle emerge.

Fig. 5(a) shows the 3D surface views of the final inhaled particle deposition patterns at mean Stokes numbers $St_{\text{mean}} = 0.04$ and 0.12, under resting condition. As expected, particle deposition, occurring mainly around the carinal ridges, increases with increasing Stokes number. But the specific deposition patterns at each carina are different. Because of the airway symmetry, particles deposit symmetrically at the first carina. However, an asymmetric particle distribution about the normal plane in the second carina is clearly displayed in zone B for $St_{\text{mean}} = 0.12$ as a result of the upstream skewed velocity profiles which cause more particles to be deposited at the inside carina. Moreover, a low particle concentration region appears at the center of the second carina. This is caused by the upstream secondary flow which moves the particles from the tube center to the top/bottom surfaces (see Fig. 3(a)). The distribution of deposited particles at the third carina (Zone C) seems to be uniform again due to the corresponding upstream uniform particle distributions under resting conditions (see Fig. 3(a)). In addition, because of the skewed velocity profiles, the *inside* third bifurcation (Fig. 1(d)) consistently collects the largest amount of wall particles compared with the *outside* third bifurcation.

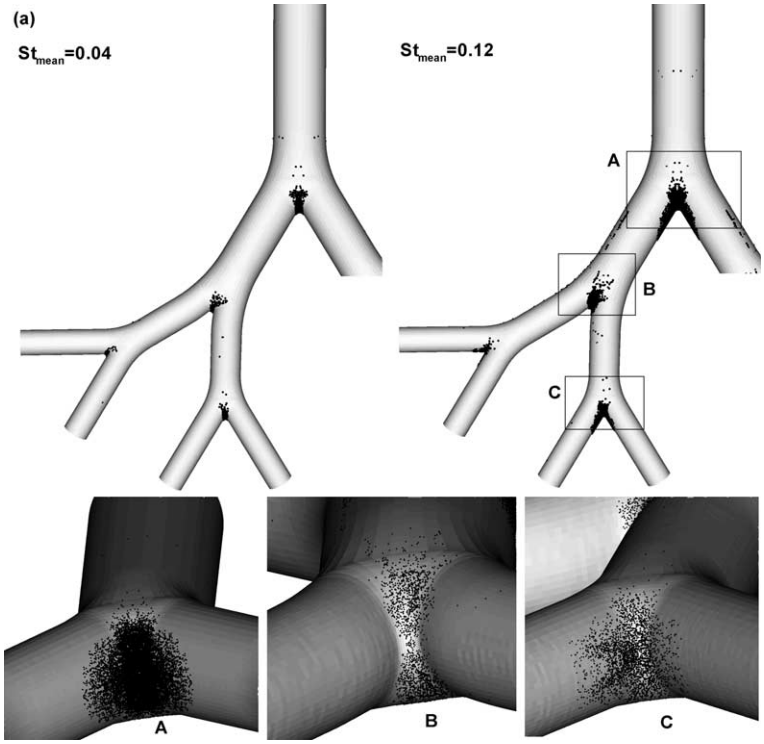

Fig. 5. 3D views of local particle deposition patterns under cyclic inhalation for: (a) resting condition; and (b) moderate exercise condition (Note: St_{mean} is the mean Stokes number evaluated at G3).

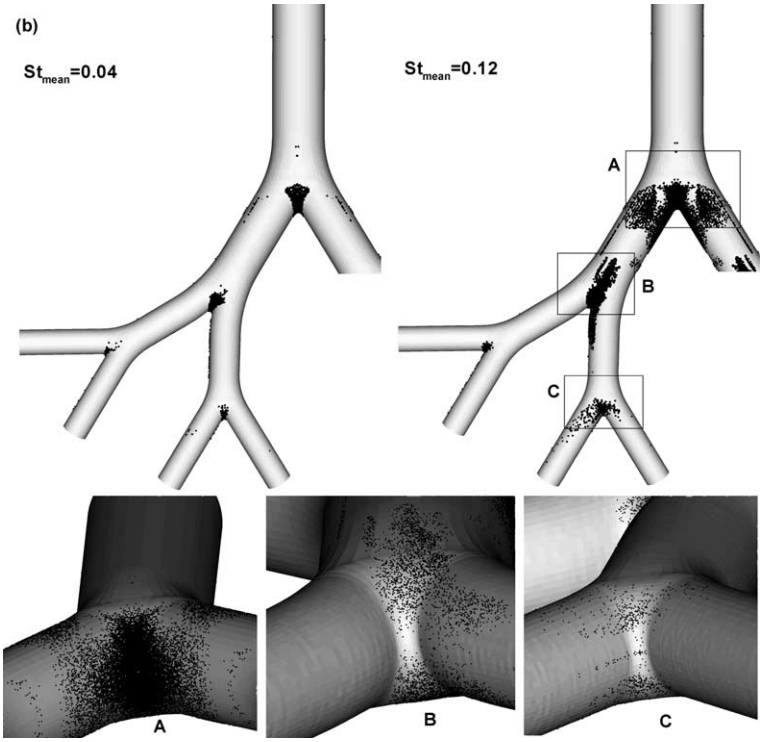

Fig. 5 (*continued*)

In the case of moderate exercise breathing (Fig. 5(b)), not only the particle deposition increases for the same mean Stokes number, but also the local deposition patterns vary, especially in the high-Stokes number case. Here, more particles deposit along the inner wall arriving from the upstream flow divider carried in the thinner shear layer. Entrained by the recirculation zone, a few particles deposit on the outside wall as well. In addition, more particles deposit upstream of the second carina because of the enlarged low-velocity zone at the tube center. The very low particle concentration zone at the *center* of the second carina (see 3D view of Zone B) is due to the distinctively low particle distribution upstream at the tube center (see Fig. 3(b)). Finally, hardly any deposited particles appear at the center of the third carina (Zone C) owing to the distinct particle-free zone upstream of the bifurcation (see Fig. 3(b)).

The particle DE, i.e., the percentage of wall particles in a given segment (cf. Fig. 1(d)) with respect to the number of incoming particles, is an important quantitative parameter which can be used to describe particle deposition in each bifurcation, zone, or generation. The effects of breathing patterns on DE at each bifurcation are shown in Fig. 6, where DE data are plotted as a function of the Stokes number and the breathing mode. It should be noted that the *St* is the *local*, *mean* Stokes number based on the parent tube diameter of a specific bifurcation and the specific respiratory waveform. The DE in the third bifurcation is the ratio of the amount of deposited particles in the entire third bifurcation including the inside and outside bifurcation to the particle

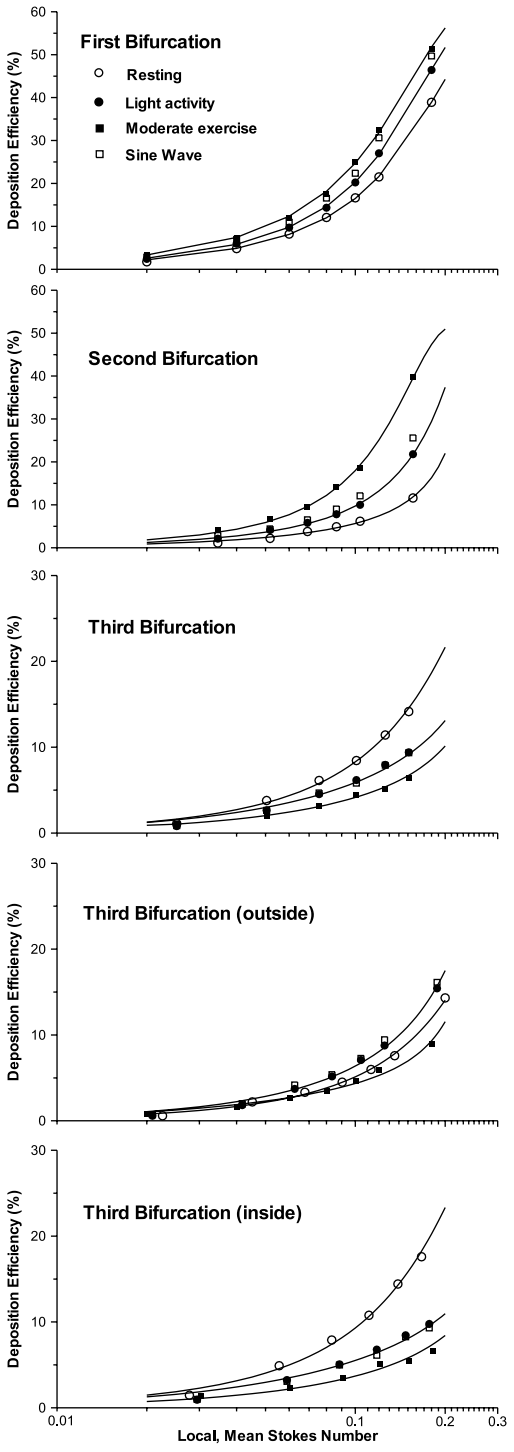

Fig. 6. Particle DEs at each bifurcation of the triple bifurcation model under cyclic inhalation condition with different breathing patterns.

number entering the entire third bifurcation. Clearly, the Stokes number is the most important factor influencing particle deposition. As mentioned, the particle DE increases with an increase in Stokes number. However, the breathing pattern (i.e., ventilation intensity) also influences particle deposition as indicated with the mean Reynolds number (Re_{mean}) which increases when the breathing patterns change from resting to light activity to moderate exercise. Hence, the DE is proportional to the mean Reynolds number in the first and second bifurcations when the particle Stokes number is fixed (Fig. 6). This may be attributed to the increase in the size of the recirculation zone at the first bifurcation, which pushes the fluid and particles towards the first carina area, and the increased vortical nature of the flow as it approaches the second bifurcation with increased Reynolds number. While for the first bifurcation the Reynolds number effect is not that noticeable, variations in DE (Re) for the second bifurcation are more pronounced. The situation is further complicated in the third bifurcation where the DE exhibits irregular variations of the mean Reynolds number (or breathing pattern). Surprisingly high DE-values occur at resting condition with relatively low mean Reynolds numbers in the *third* bifurcation, especially in the inside third bifurcation. This may be attributed to the existence of the high axial velocity region upstream of the lower third carina under resting breathing condition (see Fig. 3(a)), which induces more particles to impact the carina. The effect of breathing pattern in the outside third bifurcation is not as pronounced as in the inside one. In addition, the different *waveform* of breathing pattern (e.g., sine-waveform) has little effect on the particle deposition when the respiration rate is fixed (see Fig. 6).

3.3. Particle deposition during exhalation

The expiratory flows merge after each bifurcation, creating particle deposition patterns and efficiencies quite different from those during inspiration. Under resting and moderate exercise conditions, particles deposit mainly on the top/bottom surfaces due to secondary flows (see Fig. 7). Almost no particles deposit at the "inlet tubes" G6 because secondary flows are not set up in these straight segments. For resting conditions, particle deposition is very low at $St_{\text{mean}} = 0.04$. Only a few particles deposit at G5 and no ones at G4. This is because particles follow the secondary vortex flow well and their trajectories may not deviate from the air secondary streamlines for this low mean Reynolds and Stokes number case (Fig. 7(a)). Particle deposition increase at higher Stokes numbers under moderate exercise conditions because of stronger secondary flows leading to deviations of the (heavier) particle trajectories from the air streamlines (Fig. 7(b)).

A comparison of DE(St)-values in generations G3, G4 and G5 (cf. Fig. 1(d)) considering all three breathing patterns shown that the DEs in G5 with the well-defined inlet velocity profiles are much greater than those in G3 and G4 with more complicated flow structures due to the geometric and secondary flow effects (see Fig. 8). It also implies that double bifurcation models are, in general, insufficient to provide accurate information for aerosol deposition in the larger airways during cyclic exhalation.

Employing least-squares analysis, a comparison between particle deposition fraction in the entire four-generation airway model considering three breathing patterns is shown in Fig. 9. As expected, particle deposition during cyclic inhalation is much greater than during exhalation. The ratio of particle deposition during cyclic exhalation to inhalation is approximately 0.2.

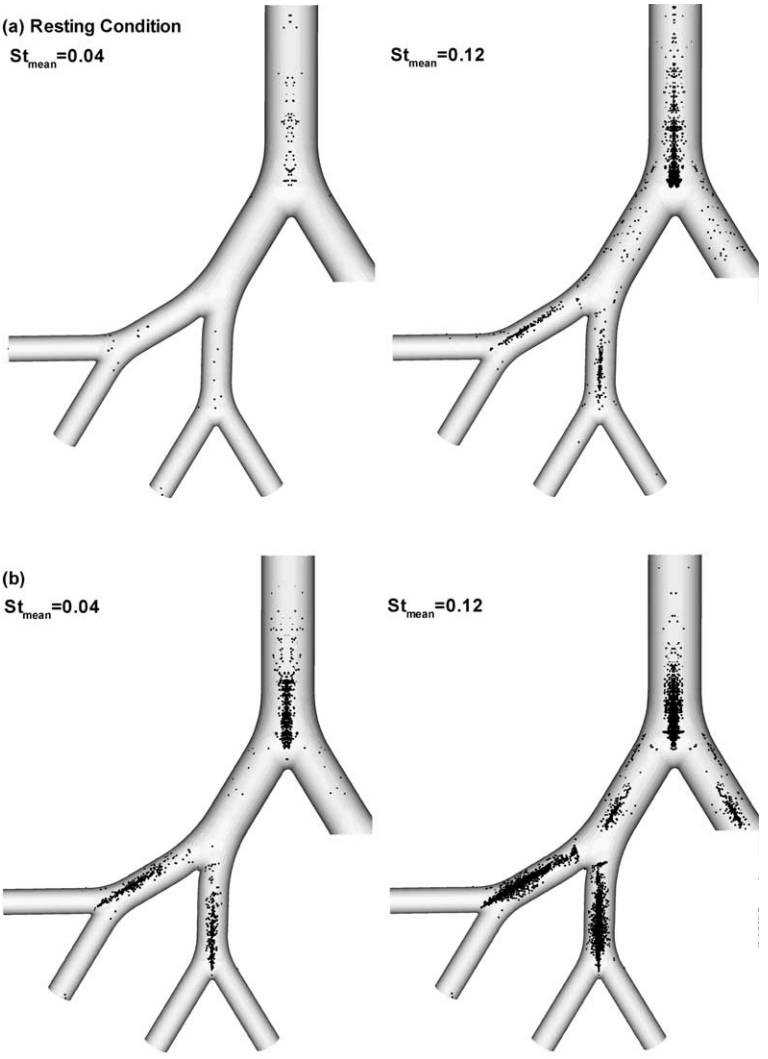

Fig. 7. 3D views of local particle deposition patterns for cyclic exhalation under: (a) resting condition; and (b) moderate exercise condition (Note: St_{mean} is the mean Stokes number evaluated at G3).

3.4. Effects of inlet conditions

So far, fully developed inlet velocity profiles and the associated particle distributions have been assumed. In order to enhance the practical value of our work, we considered skewed, time-dependent inlet velocity profiles and the corresponding inlet particle distributions for the prescribed volumetric flow rate considering a sinusoidal breathing waveform (cf. Fig. 1(a)). The skewed profiles were determined by starting a simulation at generation G1 where both inlet velocity profiles and the particle distributions are assumed to be uniform. Thus, realistic 3D air velocity profiles, particle distributions and particle velocities across the "inlet" section of tube G3 at

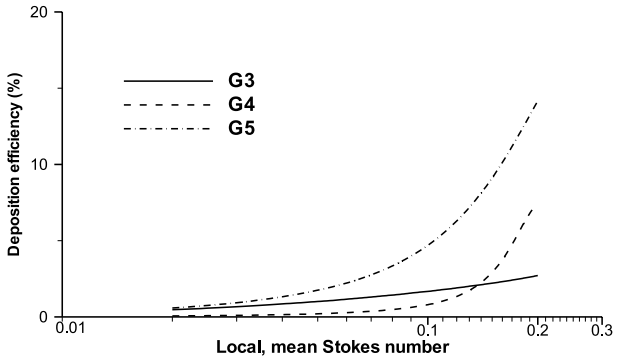

Fig. 8. Comparison of DEs at different generations for cyclic exhalation.

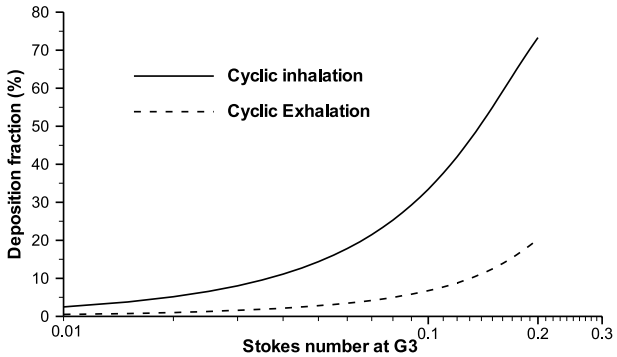

Fig. 9. Comparison of total deposition fraction in the triple bifurcation airway model between cyclic inhalation and cyclic exhalation.

different time steps were obtained and set as the inlet conditions for the simulation in the triple bifurcation unit. As expected, the velocity profiles and particle distributions are asymmetric throughout G3–G6 (Fig. 10(a)). The basic flow phenomena with asymmetric and skewed inlet conditions are similar to those with fully developed inlet profiles; that is, the air stream splits at the flow dividers forming new boundary layers along the inner walls of the daughter tubes, with the reconstruction of skewed axial velocity profiles and secondary flow induced by the subsequent changes of curvature of the nearest bifurcation (cf. Fig. 10(a) and (b)). However, the *local* air flow structures are quite different for these two cases caused by upstream effects and the interaction between axial and secondary flows. Specifically, the magnitude of axial velocity, the area and location of the maximum axial velocity zone as well as the secondary vortices and their intensity vary with the inlet flow waveform. For example, for the asymmetric inlet case, the maximum axial velocity zone becomes larger at cross-section B–B′ with a lower velocity magnitude, and the intensity of secondary flow at section D–D′ is much weaker (cf. Fig. 10(a) and (b)). Similarly, the cross-sectional particle distribution and motion are greatly influenced by the variation of local flow features and the inlet particle profiles. For example, the distinct particle-free zone at section D–D′ which appears for the fully developed inlet case cannot be observed for the skewed inlet case

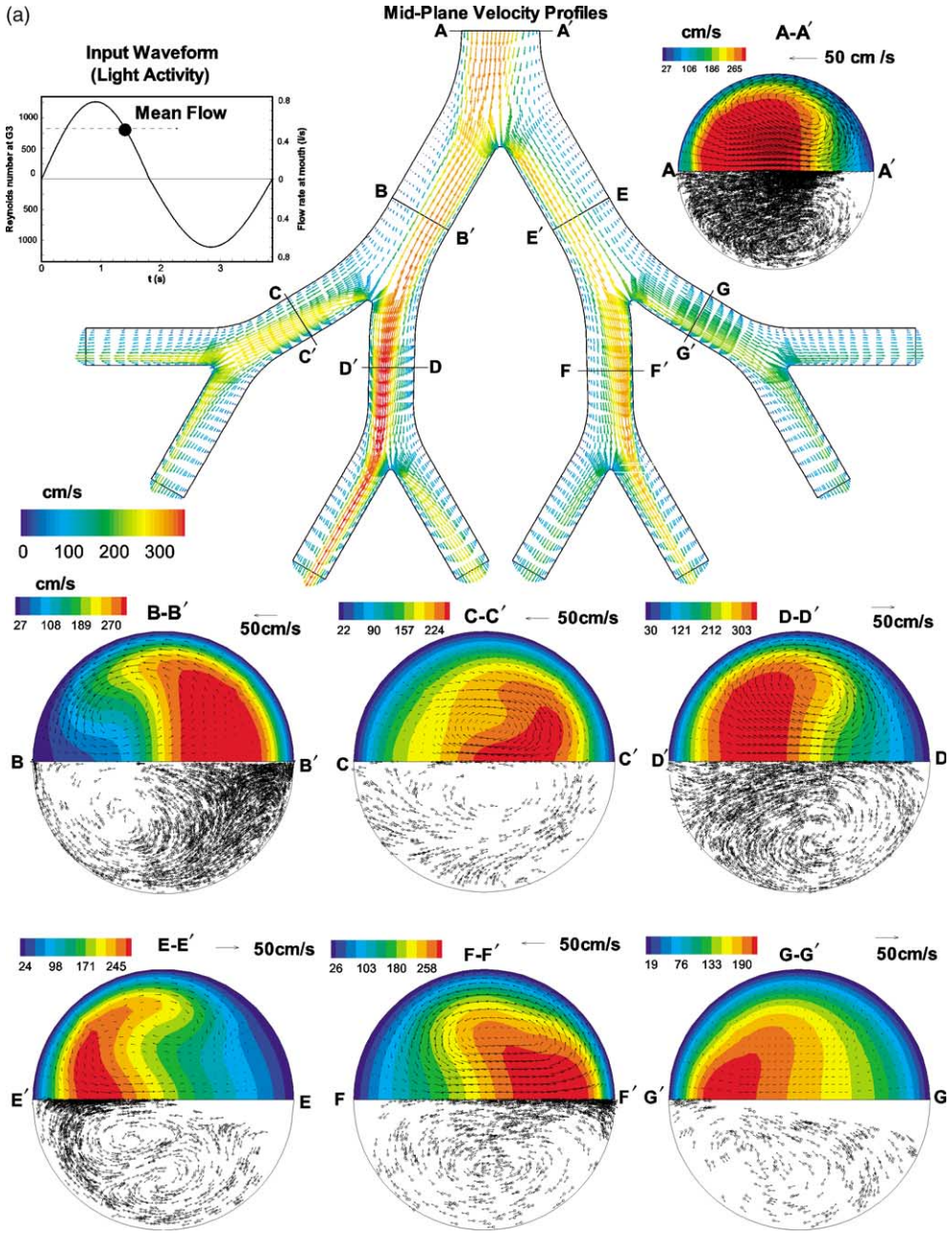

Fig. 10. Mid-plane velocity vectors, and axial velocity contours, secondary velocity vectors as well as particle distributions ($St_{\text{mean}} = 0.12$) and flow directions at selected cross-sections at the time level of mean flow rate during the decelerating inspiratory phase under light activity breathing condition for: (a) skewed inlet velocity profiles and particle distributions; and (b) fully-developed inlet velocity profiles and particle distributions.

due to the decrease of secondary flow strength. The particle-void zone near side A′ at the inlet propagates to G4 (section E–E′) and G5 (section G–G′).

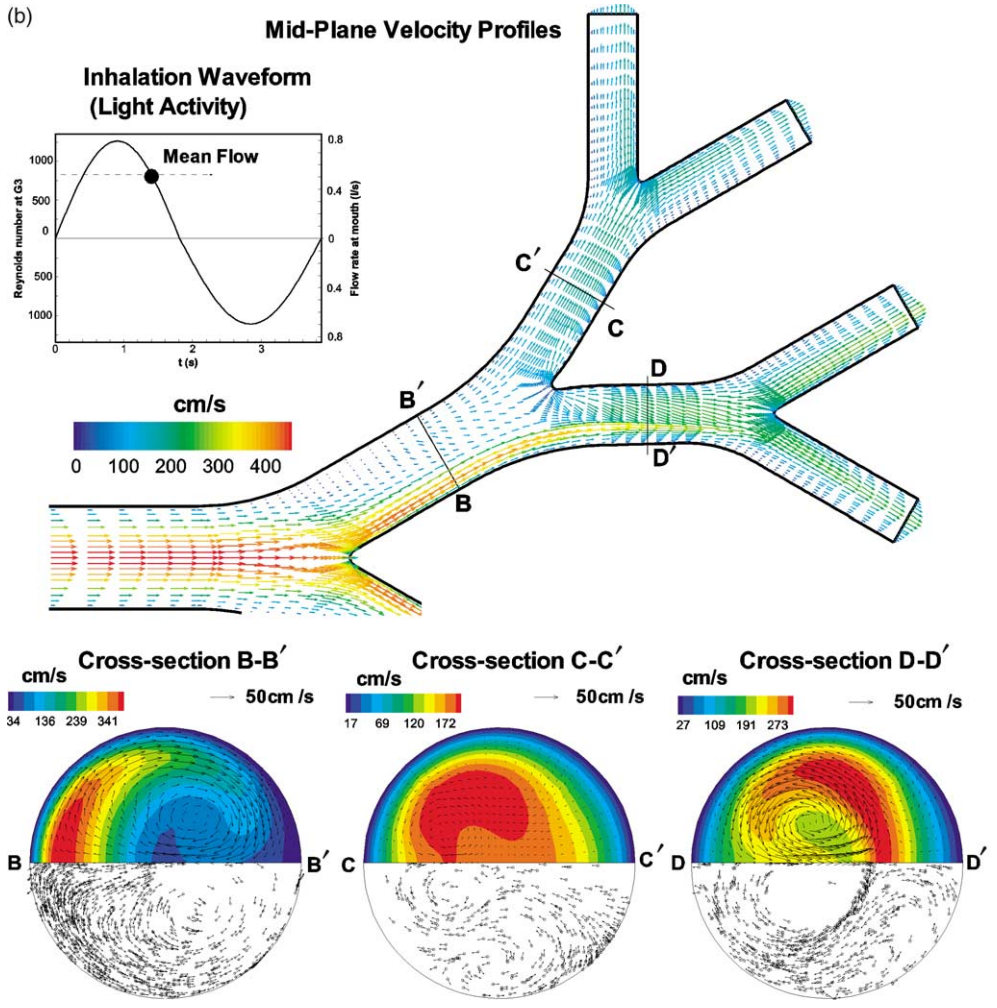

Fig. 10 (*continued*)

In summary, local particle deposition patterns are affected by the form of inlet profiles as well. Specifically, with skewed inlet velocity profiles, enhanced asymmetric distributions of deposited particles can be observed at each carinal ridge, and the low particle concentration zones at the centers of the second and third carinas are not as distinct as for the fully developed inlet case (cf. Fig. 11(a) and (b)). Comparisons of particle DEs at each bifurcation for different inlet profiles are shown in Fig. 12. As expected, the DE-values at the first bifurcation are overestimated for all mean Stokes numbers with the assumption of fully developed inlet profiles. However, the DEs at the third bifurcation for the fully developed inlet case are lower than for the skewed inlet case. Of interest is that the total DEs for the entire triple bifurcation model are almost the same for these two cases. Generally, the effect of inlet conditions on particle deposition is most pronounced for high Stokes numbers.

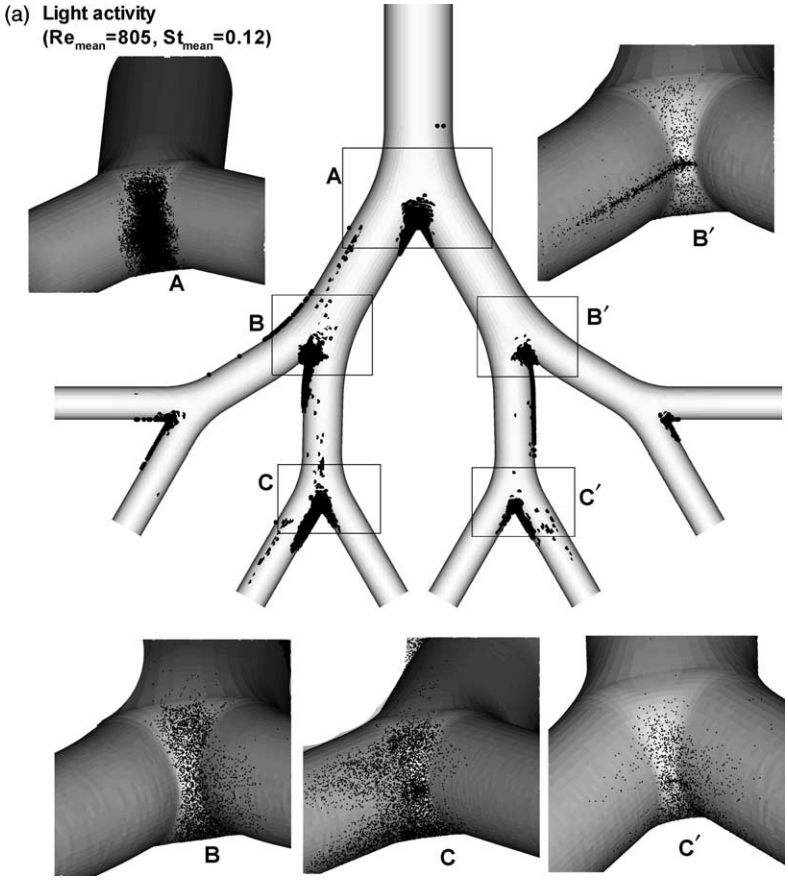

Fig. 11. 3D views of local particle deposition patterns under cyclic inhalation condition for light activity breathing at $St_{mean} = 0.12$ (Note: St_{mean} is the mean Stokes number at G3) with: (a) skewed inlet velocity profiles and particle distributions; and (b) fully developed inlet velocity profiles and particle distributions.

4. Conclusions

The effects of breathing patterns (e.g., resting, light activity and moderate exercise) on cyclic air–particle motion, local particle deposition patterns, efficiencies and fractions have been investigated numerically. The 3D simulation results show the following:

(i) Breathing patterns and hence air flow rates have a great effect on air flow structures, particle motion, deposition patterns, DEs as well as deposition fractions under both cyclic inspiration and expiration. While particles deposit mainly around the carinal ridges during inspiratory flow due to impaction, particles deposit along tubular top/bottom surfaces during exhalation because of secondary flows. However, the actual cyclic *waveform*, i.e., a given normal breathing mode vs. an equivalent sine-waveform, has only a minor effect on particle deposition.

(ii) Particle DEs may increase under cyclic flow conditions, i.e., DE-values are typically larger for cyclic flow than for steady flow at the *mean* flow rate of a given inhalation or exhalation pulse.

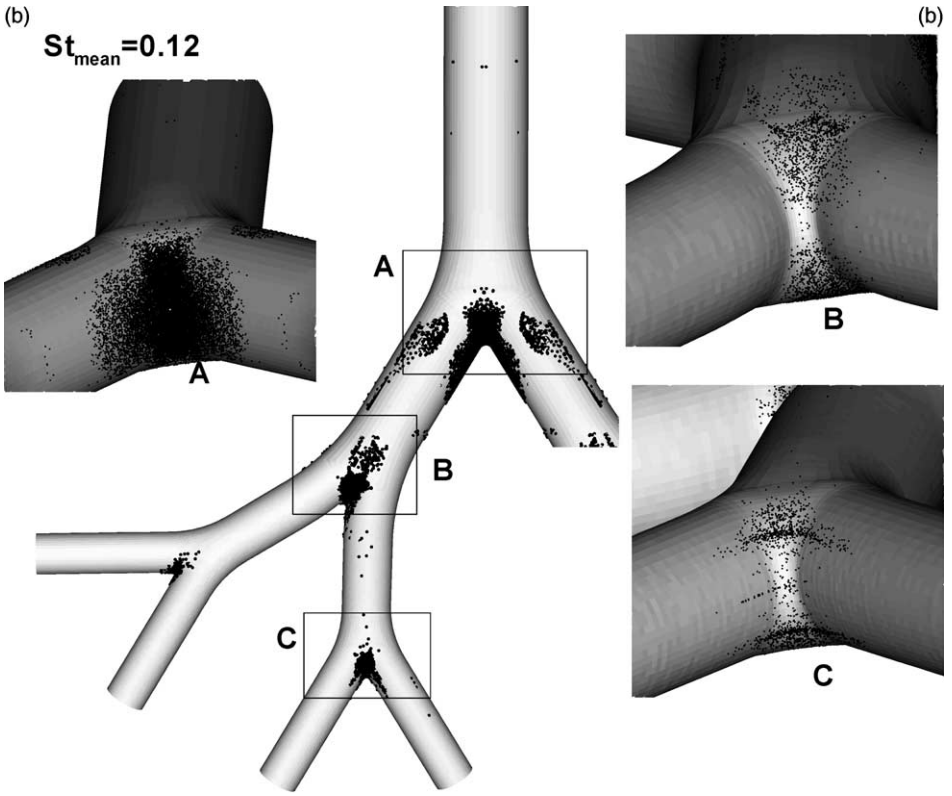

Fig. 11 (*continued*)

(iii) Under both cyclic inhalation and exhalation, the variations of particle deposition vs. Stokes number and breathing pattern in the last bifurcation or generation of the present triple bifurcation airway model are not as regular as in the upstream bifurcations or generations due to the complicated geometric and vortical flow effects. It implies that single and even double bifurcation models are insufficient to provide accurate information on particle deposition in the upper lung airways. At the same time, the form of inlet velocity profiles and particle distributions may greatly influence the local air flow structures, particle motion, particle deposition patterns as well as segmental DEs; however, overall DEs are almost the same for skewed and fully-developed inlet profiles.

(iv) Particle deposition during cyclic inhalation is up to a factor of five greater than during exhalation.

Although most bronchial bifurcations are somewhat asymmetric (Horsfield et al., 1971) and non-planar, some studies (Chang and El Masry, 1982; Tanaka et al., 1999) have shown that steady inspiratory flow in an asymmetric bifurcation exhibits the main features of the symmetric case. The investigation on non-planar geometry effects (Comer et al., 2001a, 2001b) showed that non-planar geometries only influence the flow in downstream bifurcations. For inspiration, the air

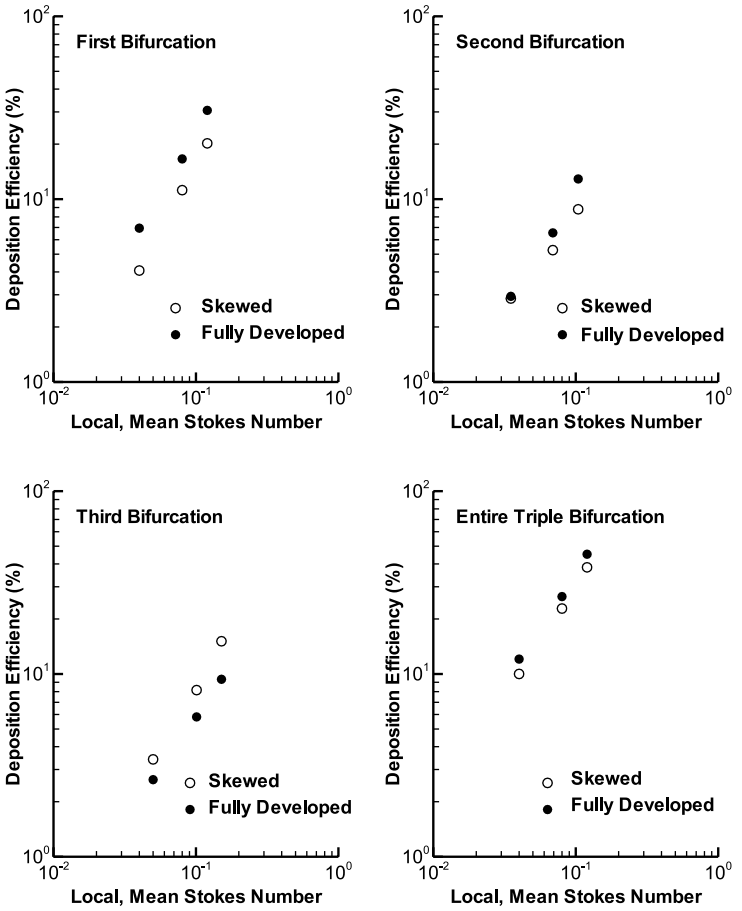

Fig. 12. Comparison of DEs at different generations under cyclic inhalation condition of light activity breathing for skewed and fully developed inlet velocity profiles and particle distributions. The DEs in the second and third bifurcation are the ratios of the amount of deposited particles in the entire second and third bifurcation to the particle number entering the entire second and third bifurcation, respectively.

and particle flow fields in the non-planar configuration resemble those in the planar configuration with profile rotations to some degree. However, particle DE values may increase slightly in out-of-plane bifurcation cases. Therefore, the present results based on the relatively ideal symmetric and planar lung airway model exhibit the essential flow features as well as particle transport and deposition phenomena encountered in human airways, with some limitations in quantitative, localized descriptions.

Acknowledgements

The use of CFX software from AEA Technology (Pittsburgh, PA), access to the SGI Origin 2400 multiprocessor workstation at the North Carolina Supercomputing Center (Research Tri-

angle Park, NC), and financial support from the US EPA as well as from the Air Force Office of Scientific Research (Dr. Walt Kozumbo, AFOSR Program Manager) are gratefully acknowledged.

References

AEA Technology, 1998. CFX-4.3: Solver. CFX International, Oxfordshire, UK.

Buchanan, J.R., 2000. Computational particle hemodynamics in the rabbit abdominal aorta. Ph.D. Thesis, Mechanical and Aerospace Engineering Department, North Carolina State University, Raleigh, NC.

Clift, R., Grace, J.R., Weber, M.E., 1978. Bubbles, Drops, and Particles. Academic Press, New York.

Chang, H.K., Masry, O.A., 1982. A model study of flow dynamics in human central airways. Part I: Axial velocity profiles. Respiration Physiology 49, 75–95.

Comer, J.K., Kleinstreuer, C., Hyun, S., Kim, C.S., 2000. Aerosol transport and deposition in sequentially bifurcating airways. ASME Journal of Biomechanical Engineering 122, 152–158.

Comer, J.K., Kleinstreuer, C., Zhang, Z., 2001a. Flow structures and particle deposition patterns in double bifurcation airway models. Part 2. Aerosol transport and deposition. Journal of Fluid Mechanics 435, 25–54.

Comer, J.K., Kleinstreuer, C., Kim, C.S., 2001b. Flow structures and particle deposition patterns in double bifurcation airway models. Part 2. Aerosol transport and deposition. Journal of Fluid Mechanics 435, 55–80.

Fenn, W.O., Rahn, H., 1965. Handbook of Physiology, Sections 3: Respiration. American Physiological Society, Washington, DC.

Hofmann, W., Balásházy, I., Koblinger, L., 1995. The effect of gravity on particle deposition patterns in bronchial airway bifurcations. Journal of Aerosol Science 26, 1161–1168.

Horsfield, K., Dart, G., Olson, D.E., Filley, G.F., Cumming, G., 1971. Models of the human bronchial tree. Applied Physiology 31, 207–217.

Katz, I.M., Martonen, T.B., 1999. A numerical study of particle motion within the human larynx and trachea. Journal of Aerosol Science 30, 173–183.

Kim, C.S., Brown, L.K., Lewars, G.G., Sackner, M.A., 1983. Deposition of aerosol particles and flow resistance in mathematical and experimental airway models. Journal of Applied Physiology: Respiration Environment Exercise Physiology 55, 154–163.

Kim, C.S., Fisher, D.M., 1999. Deposition of aerosol particles in successively bifurcating airways models. Aerosol Science and Technology 31, 198–220.

Kim, C.S., Garcia, L., 1991a. Particle deposition in cyclic bifurcating tube flow. Aerosol Science and Technology 14, 302–315.

Kim, C.S., Garcia, L., 1991b. Particle deposition in cyclic converging tube flow. Aerosol Science and Technology 14, 322–331.

Kleinstreuer, C., 1997. Engineering Fluid Dynamics—An Interdisciplinary Systems Approach. Cambridge University Press, New York.

Oho, K., Amemiya, R., 1980. Practical Fiberoptic Bronchoscopy. Igaku-Shoin, Tokyo.

Schlesinger, R.B., Gurman, J.L., Lippmann, M., 1982. Particle deposition within bronchial airways: Comparisons using constant and cyclic inspiratory flows. Annals of Occupational Hygiene 26, 47–64.

Tanaka, G., Ogata, T., Oka, K., Tanishita, K., 1999. Spatial and temporal variation of secondary flow during oscillatory flow in model human central airways. Journal of Biomechanical Engineering 121, 565–573.

Weibel, E.R., 1963. Morphometry of the Human Lung. Academic Press, New York.

Zhang, L., Asgharian, B., Anjilvel, S., 1997. Inertial deposition of particles in the human upper airway bifurcation. Aerosol Science and Technology 26, 97–110.

Zhang, Z., Kleinstreuer, C., Kim, C.S., 2000. Effects of asymmetric branch flow rates on aerosol deposition in bifurcating airways. Journal of Medical Engineering and Technology 24, 192–202.

Zhang, Z., Kleinstreuer, C., 2001. Effect of particle inlet distribution on deposition in a triple bifurcation lung airway model. Journal of Aerosol Medicine 14, 13–29.